Check for updates

Position-Selective Introduction of Ferromagnetism on the Micro- and Nanoscale in a Paramagnetic Thin Palladium Film

Petter Ström, Christina Vantaraki, Rajdeep Kaur, Tuan T. Tran, Gyula Nagy, Vassilios Kapaklis, and Daniel Primetzhofer*

Postsynthetic, position-selective addition of properties to materials constitutes a paradigm shifting step in materials engineering. The approach enables creation of material systems inaccessible by equilibrium and near-equilibrium synthesis and can be applied in novel practical applications as well as fundamental physics studies over a range of length and energy scales. Ion implantation is a versatile, scalable, industry-compatible tool, enabling the next step in this development. Herein, ion implantation is used to design and functionalize a mesoscopic magnetic architecture. A self-supporting mask is combined with implantation of 60 keV Fe ions to create an embedded array of ≈8 μm-wide circular ferromagnetic regions in a Pd film. The approach is contactless, free from surface residues, and requires no focusing or scanning of the beam. Magnetic properties of the array are probed with longitudinal magneto-optic Kerr effect measurement while varying sample temperature and applied magnetic field. Microstructures are visualized with Kerr microscopy and compared to the Fe distribution measured with microbeam proton-induced X-Ray emission. Sample topography after implantation is obtained by atomic force microscopy, while ion beam analysis is used to probe concentration depth profiles of implanted Fe, impurities, and to investigate material mixing.

1. Introduction

Scalable, noncontact methods to locally add properties in materials, with position control in 3D, are game changing for our ability to create highly complex engineered material systems. Areas of interest include functionally graded materials and other hybrid materials,[1–3] as well as a plethora of applications where individual elements featuring distinct properties on the nanoscale are important. One example of a class of such applications is adaptive, so called intelligent materials.[4,5] In general, materials with spatially dependent properties are of significant interest for components produced via, for example, additive manufacturing.[6] A multitude of methods will certainly be involved in the development and fabrication of these materials and components. Here we focus on ion implantation. As a far-from-equilibrium, postsynthesis sample processing method, it provides unique possibilities for creating structures with modified properties whose geometries cannot be easily obtained via standard additive manufacturing techniques.

Ion implantation is a well-established process tool in the semiconductor industry. By subsequent steps of photoresist masking and up to a few dozen implants performed with a range of ions at energies from around 100 eV to 10 MeV, dopants are introduced locally to form the different regions of complementary metal oxide semiconductor devices.[7–10] As such, all modern digital electronics are dependent on manufacturing steps involving ion implantation, and it has been widely adopted as a tool for local tailoring of dopant concentrations. However, the versatility of the method is not fully exploited with this single, albeit thoroughly developed, application. Rather, as already hinted above, it can be applied at the forefront of new materials engineering, to perform localized property modification. A specific application for the property-enhanced structures enabled by ion implantation is found in synthesis of magnetic materials.

Artificial magnetic structures on the micro- and nanoscale have been emerging over the last few decades as systems of interest for applications in spintronics[11,12] as well as studies of emergent physics in, for example, magnetic metamaterials.[13–18] Ongoing development relevant to both these fields includes advancing from 2D magnetic patterns to more complex 3D structures.[19] Several types of 3D magnetic nanostructures have already been studied. These include self-assembled

P. Ström, R. Kaur, T. T. Tran, G. Nagy, D. Primetzhofer
Applied Nuclear Physics
Department of Physics and Astronomy
Uppsala University
Box 516, Uppsala 751 20, Sweden
E-mail: petter.strom@physics.uu.se

C. Vantaraki, V. Kapaklis
Materials Physics
Department of Physics and Astronomy
Uppsala University
Box 516, Uppsala 751 20, Sweden

D. Primetzhofer
Tandem Laboratory
Uppsala University
Box 529, Uppsala 751 21, Sweden

The ORCID identification number(s) for the author(s) of this article can be found under https://doi.org/10.1002/pssr.202400053.

DOI: 10.1002/pssr.202400053

 © 2024 Wiley-VCH GmbH

structures,[20,21] as well as those produced via microstereolitography or 3D microprinting with incorporation of magnetic nanoparticles,[22,23] focused electron beam induced deposition,[19,24] and two-photon optical lithography.[25] While the unique advantages offered by these production methods are discussed in detail in the studies in question, we note that ion implantation stands out in being simultaneously scalable, postsynthetic, position selective with nm scale resolution, and enabling contactless sample processing with available industrial tools.

Magnetic property modification by ion irradiation and implantation has been discussed in previous work.[26] Possible methods for such modification include introduction of a ferromagnetic micropattern in a paramagnetic matrix via Ga-ion irradiation of a $Fe_{60}Al_{40}$ alloy with a focused ion beam (FIB). While such a methodology is reminiscent of that applied in the present work, it is limited in terms of scalability, versatility, and maximal affected sample depth. The limitation in scalability comes from the serial nature of FIB patterning and the limitation in versatility from the fact that the employed ion beam needs to be compatible with a focused source, for example, a liquid metal ion source. Finally, the sample depth limitation is set by the upper limit in beam energy that can be technically combined with the focusing requirement. All these limitations are alleviated by turning to masked implantation using a general-purpose industrial ion implanter. The geometry of implanted structures is then controlled laterally via the geometry of the mask, and in the depth direction by the properties of the employed ion beam, thus enabling 3D shape control. We further note that masked ion implantation can constitute a synthesis path for magnetic structures that do not significantly modify the sample surface topography. See also the study by Fassbender et al.[27] and several references therein, where the minimal effect on surface topography in magnetic patterning via ion implantation is discussed. If the mask is self-supporting, rather than deposited onto the sample, surface contamination related to, for example, photoresist masking may be reduced.

Implantation of Cr^+ ions into $Ni_{80}Fe_{20}$ permalloy samples patterned via use of a lithographic mask constitutes an example of magnetic property modification via masked ion implantation.[28] More specifically, the Curie temperature was locally decreased due to the implantation, to create paramagnetic regions in the ferromagnetic matrix material. The effect has also been applied for frequency tuning in magnetic vortex-based oscillators relevant for, for example, wireless communication applications.[29] Furthermore, defect-induced ferromagnetism in oxide semiconductors,[30] introduction of hard regions in a soft ferromagnetic, amorphous matrix,[31] and local removal of the ferromagnetic property in FePt or FePd bit patterned storage media[32] have all been discussed in the literature and realized by means of ion implantation. However, in relation to the latter example involving FePt and FePd, we perceive that the introduction of ferromagnetism in spatially limited regions through local composition modification by implantation has not been thoroughly investigated. While we have previously demonstrated that the magnetic properties of a Pd film implanted with $^{56}Fe^+$ ions can be locally tuned via the Fe concentration on a nm scale,[33] said concentration was only varied in the depth direction of the sample. In the present work, we combine the technique from ref. [33] with the use of a self-supporting mask to achieve patterned, contactless ion implantation. The result is an embedded array of microscopic ferromagnetic Fe-containing disks in the Pd matrix, with estimated edge sharpness on the order of 20 nanometers. Both the magnetic properties of these disks and the effect on sample surface topography are investigated, helping to pave the way for predictable and precise magnetic micro- and nanopatterning with ion beams. The demonstrated methodology can be extended into a versatile approach for creation of complex repeating 3D patterns by successive ion implantations at different energies, using different implanted elements combined with different masks.

2. Results

A 100 nm Pd film was prepared on a $(1\bar{1}02)$-oriented Al_2O_3 substrate by magnetron sputter deposition. 4.7 nm of Al was deposited on top of this film and oxidized upon removal of the sample from the sputter chamber, forming ≈6 nm of Al_2O_3. This top film served as a protection layer with decreased sputter yield during the subsequent Fe implantation, which was carried out with 60 keV $^{56}Fe^+$ ions. A mask consisting of a copper G2000HA Gilder transmission electron microscopy (TEM) grid, featuring 6.5 μm circular holes in a hexagonal pattern with 12.5 μm pitch, was clamped onto the sample during implantation. An implantation pattern corresponding to the pattern of the grid was thus generated in the sample. A fluence of 1.7×10^{16} Fe ions cm^{-2} was applied. The edge geometry of the grid yielded an opening width of the holes at the side facing the sample of ≈8 μm, defining the lateral size of implanted structures. **Figure 1**A gives a representative scanning electron microscopy (SEM) image obtained on the patterned sample. Contrast is observed between the regions where Fe ions have been implanted (bright) and the

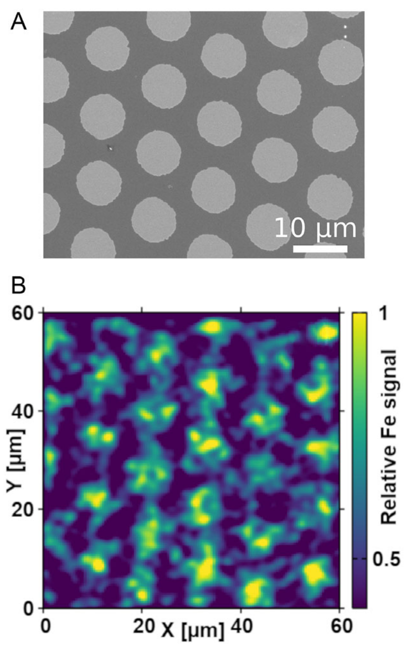

Figure 1. A) SEM image and B) μ-beam PIXE map of relative Fe concentration, for an array of microstructures produced by implantation of $^{56}Fe^+$ ions into a Pd film through a mask with circular openings.

18626270, 2024, 8, Downloaded from https://onlinelibrary.wiley.com/doi/10.1002/pssr.202400053 by Uppsala University Library, Wiley Online Library on [12/08/2024]. See the Terms and Conditions (https://onlinelibrary.wiley.com/terms-and-conditions) on Wiley Online Library for rules of use; OA articles are governed by the applicable Creative Commons License

regions that were covered by the ribs of the masking TEM grid during implantation (dark). An Fe concentration map measured with microbeam particle-induced X-Ray emission (μ-beam PIXE), shown in Figure 1B, further corroborates the statement that Fe is implanted according to the pattern of the mask. The Fe map appears as an array of ≈8 μm-wide implanted circles, although the edges of the structures are not well-resolved by the μ-beam measurement. The latter fact is explained by a combination of limited data collection statistics and a probing beam spot size of lateral width on the order of 3–5 μm.

Macroscopic magnetic properties of the microstructure array were probed via a longitudinal magneto-optic Kerr effect (L-MOKE) measurement. L-MOKE signals representative of the collective magnetic response of the array at temperatures of 115 and 15 K are given in **Figure 2**A and Figure 2B respectively. Similarly to the case for a film implanted without mask in the study by Ström et al.[33] soft ferromagnetic behavior at low temperature, with a coercivity of a few mT, is indicated. We note that both saturation magnetization and coercivity increase with decreasing temperature. The origin of the ferromagnetism in Fe-implanted Pd is further discussed in the study by Ström et al.[33] Although the total amount of implanted material is small, the peak Fe concentration is ≈8.5 at.%, resulting in a narrow region of sample

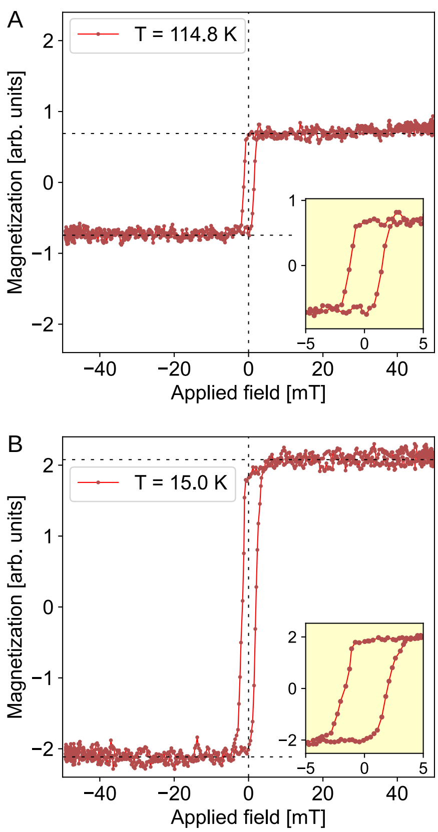

Figure 2. Hysteresis curves recorded by L-MOKE, with in-plane applied magnetic field for array of 8 μm-wide $^{56}Fe^{+}$ ion-implanted disks in Pd at A) 115 K and B) 15 K. The insets contain magnifications of the applied field range from −5 to +5 mT, while dashed lines mark the position of zero field and the saturation magnetization on the positive and negative branch.

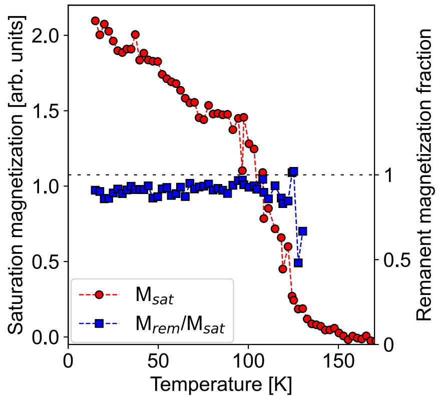

Figure 3. Temperature scaling of the implanted array's saturation magnetization and ratio of remanent to saturated magnetization.

material in which robust, low-temperature ferromagnetism is expected to occur.

In **Figure 3**, the saturation magnetization of the array is given as a function of temperature, along with the ratio of remanent to saturated magnetization ($M_{\mathrm{rem}}/M_{\mathrm{sat}}$). A reasonably distinct paramagnetic–ferromagnetic phase transition is observed at ≈120 K. The ratio $M_{\mathrm{rem}}/M_{\mathrm{sat}}$ persists at a value close to 1 all the way up to the transition temperature, indicating that magnetization noncollinearities within the disks are not present or dominant. As such, we conclude that the structures at the size scale produced in the present case are collinearly magnetized, and no evidence for vortices is observed. The extended tailing of the saturation magnetization curve at temperatures above the critical temperature is an indication of sizable magnetic susceptibility of the disk structures. This is a characteristic property of magnetic systems composed of thin layers of Fe embedded in Pd matrices, with further details reported in previous works.[34,35]

The magnetic property measurements are complemented in **Figure 4** with a MOKE microscopy image at 90 K, obtained as the difference between a reference image at −2 mT and a recorded image at 2 mT applied field. The magnetic contrast between the implanted regions and the regions covered by the

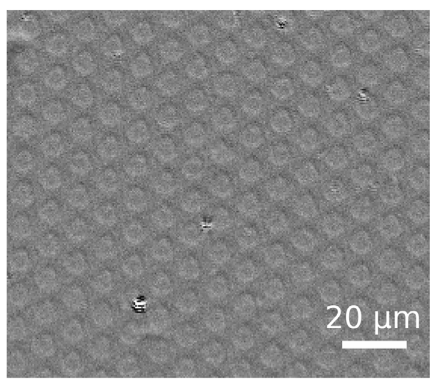

Figure 4. Magnetic contrast, as observed with MOKE microscopy on implanted array at 90 K, by mapping the pixel-wise difference in recorded intensity between the cases of −2 and +2 mT in-plane applied magnetic field.

18626270, 2024, 8, Downloaded from https://onlinelibrary.wiley.com/doi/10.1002/pssr.202400053 by Uppsala University Library, Wiley Online Library on [12/08/2024]. See the Terms and Conditions (https://onlinelibrary.wiley.com/terms-and-conditions) on Wiley Online Library for rules of use; OA articles are governed by the applicable Creative Commons License

TEM grid ribs is clear and reflects the implantation pattern from Figure 1. Note, however, that the resolution of the image in Figure 4 is limited by the optical microscope with which it was obtained, and does not reflect the edge sharpness of the implanted structures. A video showing a running average of the reference-subtracted Kerr microscopy image obtained while switching the applied field between −2 and 2 mT is provided along with the Supporting Information for this article. Contrast is observed to appear and disappear, although out of sync with the field switching due to the averaging over several subsequently acquired frames.

Atomic force microscopy (AFM) was performed in contact mode at room temperature to map the sample surface topography. As explicitly shown in Figure 3, the implanted structures are not ferromagnetic at this temperature, eliminating the possible effect of magnetic contrast on the resulting data. The AFM map shown in **Figure 5** demonstrates that the sample surface is not entirely flat after ion implantation. That observation is not unexpected. Given a sputter yield for the top Al_2O_3 layer of ≈1.8 atoms per incoming Fe ion, as measured in the study by Ström et al.[33] we would expect the surface to recess by 2.6 nm in the implanted regions. By extracting a height profile across the edges of the circular structures observed with AFM, we obtain a step height rather on the order of 1–2 nm. The fact that the value is lower than that obtained by simply calculating the amount of sputtered material can be explained by slight swelling of the sample due to the added Fe atoms inside the implanted regions.

Ion beam composition analysis (IBA) in the form of Rutherford backscattering spectrometry (RBS) and time-of-flight elastic recoil detection analysis was performed on a reference sample (referred as *IBA reference sample*), sputtered in the same batch as the patterned sample. The reference was implanted under similar conditions as the patterned sample, but without mask, to provide the possibility to verify the Fe concentration depth profile. In addition, the IBA measurements enabled investigation of impurity fractions in the film as well as material mixing induced at the layer interfaces by the implantation. To emphasize the latter effect, a slightly higher ion beam current and total ion fluence was employed for the reference sample as compared to the patterned sample. Collected data and, in the case of RBS, a calculated spectrum based on an adapted sample composition are displayed in Figure S1 of the Supporting Information for this article. The analysis, discussed in further detail in the Supporting Information, reveals a film of acceptable composition and quality with 0.4 at.% of C impurity, limited material mixing, a total amount of implanted material within ±1.5% of the target fluence, an expected Fe concentration depth profile, and predictable removal of the Al_2O_3 sputter protect layer.

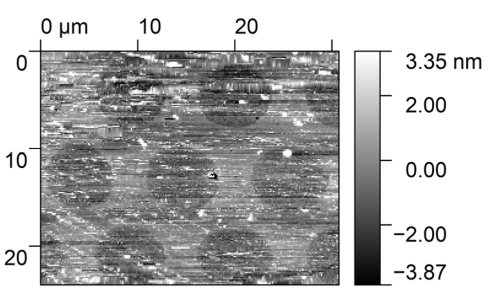

Figure 5. Topographic AFM map showing a measurable height difference of 1–2 nm between ion-implanted circular regions and the surrounding nonimplanted surface.

In order to assess the limit in edge sharpness for the structures treated in the present work due to lateral straggling of the ions entering the sample matter, a Monte Carlo simulation was carried out. Details are provided in the Supporting Information. The result is that 60 keV $^{56}Fe^{+}$ ions impinging at normal incidence on a single point of the sample surface will spread out, with average displacement of 7.4 nm along a given direction perpendicular to the implantation axis. Figure S2A of the Supporting Information shows the distribution of implanted Fe atoms and in Figure S2B a convolution of the lateral projection of that distribution and a step function representing an ideal mask edge is given. The latter provides an estimation of the variation in implanted Fe concentration near the mask edge and reveals a broadening of the resulting structure edge on the size scale of 20 nm.

3. Discussion

While a single energy was applied for ion implantation in this work, extension to several subsequent implantations to different depths is possible for generating 3D microstructure arrays. Further flexibility in structure positioning can be added by careful repositioning of the mask. If surface flatness is critical on the nm level, an appropriately thick sputter protect layer can be deposited on the sample through the same mask as used for the subsequent ion implantation. The thickness of the layer is, in such a case, selected so that it is just barely removed by sputtering during the implantation. This approach leaves sample swelling as the only effect modifying the surface topography. A resulting flatness within ± 1 nm is then considered feasible, given that the initial film is similarly flat.

As noted above, some material mixing was observed with IBA after ion implantation on the IBA reference sample in this work. The effect was, however, limited. We note that increased material mixing would be expected for larger ion fluences, larger beam currents, and lower beam energies. The latter is due to the fact that lower energy leads to an implantation depth profile peaked closer to the sample surface, with a larger energy deposition in elastic collisions with target nuclei for the incoming ions at the interface between the sputter protect layer and the underlying film. Material mixing is in turn expected to somewhat hamper the paramagnetic–ferromagnetic transition in the implanted regions in a similar manner as observed for substrate interface mixing in the study by Ström et al.[33] Finally, such mixing may also lead to direct exposure of the underlying film to the ion beam before all the material in the sputter protect layer is consumed, thus increasing unwanted sputtering of the film and the ions already implanted into it. These facts need to be taken into consideration when designing robust implantation schemes for sample property modification.

When comparing the scaling of saturation magnetization with temperature (Figure 3) in the present work to that obtained on films implanted without mask in the study by Ström et al.[33] a more step-like paramagnetic–ferromagnetic transition can be

 © 2024 Wiley-VCH GmbH

18626270, 2024, 8, Downloaded from https://onlinelibrary.wiley.com/doi/10.1002/pssr.202400053 by Uppsala University Library, Wiley Online Library on [12/08/2024]. See the Terms and Conditions (https://onlinelibrary.wiley.com/terms-and-conditions) on Wiley Online Library for rules of use; OA articles are governed by the applicable Creative Commons License

perceived in the present case. There are several factors that contribute to this subtle difference, including film purity and crystal quality. Part of the explanation may also lie in the differences in magnetic property measurements. The SQUID magnetometer used in the referenced work is sensitive to the sample magnetic moment over the entire Fe-implantation depth profile, while the MOKE measurements applied here are affected by a light penetration depth on the order of 30 nm. The latter therefore exclude the effect of the low-concentration tail beneath the implanted Fe concentration peak on the obtained data, which would be expected to yield the observed behavior. A thorough description of the impact of the low-concentration tail on the total magnetization of an Fe-implanted Pd film is provided in the study by Ström et al.[33] The model developed in that work assumes that each region of the film contributes to (and increases) the total magnetization of the sample at temperatures below the paramagnetic–ferromagnetic transition temperature associated with the local Fe concentration. As such, while a measurement sensitive to the entire distribution is expected to yield slightly increased magnetization values at temperatures below the transition temperature, we do not expect that the application of MOKE rather than SQUID magnetometry yields a qualitative difference in the recorded hysteresis loops (Figure 2).

Although the structures produced in the present work possess magnetic properties similar to those in a film where the implantation is laterally continuous, the fact that straggling is limited makes it feasible to generate significantly smaller structures with a similar methodology. On size scales down to $\approx$100 nm, edge broadening on the order of 20 nm is not a critical problem when attempting to maintain control of implanted structure geometries. Both size and shape effects on the resulting magnetic properties are expected on those scales. It should be noted here that the edge quality of the mask constitutes a limit for the edge quality of any implanted structure. Beam divergence may also be expected to contribute, especially in cases where the distance between the mask and the sample surface is similar to the desired edge sharpness or larger. Ion diffraction is, however, not expected to be limiting for the size scales and ion properties of interest in the present context (see, e.g., a study by Winter and Schüller[36]).

4. Conclusion

Ion implantation presents yet untapped opportunities for localized modification of material properties with 3D position selectivity, here exemplified by an array of circular ferromagnetic elements created in a paramagnetic Pd film by Fe-ion implantation. Robust, predictable results in terms of the Fe concentration distribution (both laterally and with depth) and magnetic properties, low impurity concentrations, and limited material mixing were demonstrated. The minimal lateral position resolution achievable with the applied implantation methodology is determined by the producible mask quality, ability to keep a minimal distance between the mask and the sample, as well as ion directional straggling. As an example, for the 60 keV $^{56}Fe^{+}$-ion implantation used here, ions impinging on the same point of the target surface spread out over an implantation plume with a lateral radius of $\approx$20 nm. The resulting size scale limitation is comparable to the lateral size allowance of a single bit on a state-of the art hard disk drive ($\approx$25 nm for an areal information density of 1 Tb in^{-2}, see, e.g., the work by Dwivedi et al.[37]). For structure sizes on the order of hundreds of nm, edge broadening can be compensated for by a corresponding size decrease of the mask openings that define the desired geometries.

5. Experimental Section

Sample Preparation: Magnetron sputter deposition was performed in a UHV system, where the background pressure before the beginning of the deposition procedure was 5×10^{-9} mbar. The working gas during sputter operation was Ar at 5.5×10^{-3} mbar. A discharge power of 50 W was employed for both Al and Pd, with corresponding discharge voltages of 337 and 333 V respectively. Ion implantation was carried out at the 350 kV ion implanter of the Uppsala Tandem Laboratory,[38] with 60 keV $^{56}Fe^{+}$ ions. The current density impinging on the patterned sample was 0.17 μA cm^{-2}, and the total ion fluence was 1.7×10^{16} Fe ions cm^{-2}. For the IBA reference sample (see further details in Supporting Information), the current density was 0.39 μA cm^{-2} and ion fluence was 2×10^{16} Fe ions cm^{-2}.

μ-Beam PIXE Analysis: The lateral Fe distribution on the patterned sample was measured by means of μ-beam PIXE with a 2 MeV p^{+} beam at the Tandem Laboratory light ion microprobe setup.[39] Raw μ-beam data was processed using GeoPIXE[40] in order to generate a map of relative Fe abundance.

Magnetic Property Measurements: L-MOKE measurements were carried out using a laser beam with an illumination area of $\approx$1 mm^2 centered on the ion-implanted region and with an incidence angle of 45°. Data was acquired while sweeping the in-plane applied magnetic field from -50 to $+50$ mT and varying the sample temperature from 15 to 170 K. To calculate the saturation magnetization, the average absolute value of the L-MOKE signal intensity between applied fields of 10 and 20 mT was extracted on the positive and negative applied field branch separately. The saturation value was then defined as the average of these averages. Remanent magnetization was also defined separately for the positive and negative branches and averaged to yield the reported data. For the positive branch, a line was fit to the L-MOKE signal intensity between -0.5 and $+1.5$ mT and the remanent magnetization was taken as the y-axis intersect of that line. For the negative branch, the fit was performed between -1.5 and $+0.5$ mT.

Magnetic contrast between the implanted microstructures and the surrounding matrix material was verified with MOKE microscopy, once again using the longitudinal configuration. In order to isolate the magnetic contrast in the obtained MOKE microscope images, and filter out contrast due to sample surface topography, a reference image was initially obtained at a set value of the in-plane applied field. The field was then switched from the reference value to a measurement value, and the pixel-wise difference in image intensity was recorded. For the still image in Figure 4, the reference field was -2 mT and the measurement field was 2 mT. In order to generate a magnetic contrast video, a running pixel-by-pixel average of the difference between the measured image intensity and the reference intensity was continuously acquired while switching the field back and forth between the reference and measurement values.

Atomic Force Microscopy: AFM was performed in contact mode at room temperature (where the implanted structures were not ferromagnetic), using a PSIA XE150 AFM, to map the sample surface topography. The recorded topography data was processed with Gwyddion 2.56[41] for row-alignment, scar correction, and height offset subtraction.

Supporting Information

Supporting Information is available from the Wiley Online Library or from the author.

© 2024 Wiley-VCH GmbH

18626270, 2024, 8, Downloaded from https://onlinelibrary.wiley.com/doi/10.1002/pssr.202400053 by Uppsala University Library, Wiley Online Library on [12/08/2024]. See the Terms and Conditions (https://onlinelibrary.wiley.com/terms-and-conditions) on Wiley Online Library for rules of use; OA articles are governed by the applicable Creative Commons License

Acknowledgements

The authors would like to thank Johan Oscarsson and Mauricio Sortica at the Uppsala Tandem Laboratory for help with ion implantations and Rimantas Brucas at MyFab Uppsala for assistance in sample cutting. Gabriella Andersson at Uppsala University further provided assistance with MOKE microscopy. The authors are thankful for an infrastructure grant by VR-RFI (grant number 2019_00191) supporting accelerator operation. Authors V.K. and C.V. acknowledge support from the Swedish Research Council (project no. 2019-03581). C.V. further gratefully acknowledges financial support from the Colonias-Jansson Foundation, Thelin-Gertrud Foundation, and Liljewalch Foundation.

Conflict of Interest

The authors declare no conflict of interest.

Data Availability Statement

The data that support the findings of this study are available from the corresponding author upon reasonable request.

Keywords

ion implantations, magnetic microstructures, magnetic thin films, materials engineering, position-selective materials modifications

Received: February 14, 2024
Revised: March 25, 2024
Published online: April 9, 2024

[1] B. Kieback, A. Neubrand, H. Riedel, *Mater. Sci. Eng. A* **2003**, *362*, 81.
[2] B. Saleh, J. Jiang, R. Fathi, T. Al-hababi, Q. Xu, L. Wang, D. Song, A. Ma, *Composites, Part B* **2020**, *201*, 108376.
[3] F. Barthelat, M. Mirkhalaf, *J. R. Soc. Interface* **2013**, *10*, 20130711.
[4] A. Walther, *Adv. Mater.* **2020**, *32*, 1905111.
[5] C. Kaspar, B. J. Ravoo, W. G. van der Wiel, S. V. Wegner, W. H. P. Pernice, *Nature* **2021**, *594*, 345.
[6] S. Tammas-Williams, I. Todd, *Scr. Mater.* **2017**, *135*, 105.
[7] M. Nastasi, J. W. Mayer, in *Ion Implantation and Synthesis of Materials*, Springer-Verlag Berlin Heidelberg, Germany **2006**.
[8] K. Tsukamoto, T. Kuroi, Y. Kawasaki, *AIP Conf. Proc.* **2011**, *1321*, 9.
[9] M. I. Current, in *Industrial Accelerators and their Applications* (Eds: R. W. Hamm, M. E. Hamm), World Scientific Publishing Co., Singapore **2004**.
[10] M. I. Current, *Mater. Sci. Semicond. Process.* **2017**, *62*, 13.
[11] A. Hoffmann, S. D. Bader, *Phys. Rev. Appl.* **2015**, *4*, 047001.
[12] R. Wiesendanger, *Nat. Rev. Mater.* **2016**, *1*, 16044.
[13] C. Nisoli, R. Moessner, P. Schiffer, *Rev. Mod. Phys.* **2013**, *85*, 1473.
[14] L. J. Heyderman, R. L. Stamps, *J. Phys. Condens. Matter* **2013**, *25*, 363201.
[15] V. Kapaklis, U. B. Arnalds, A. Farhan, R. V. Chopdekar, A. Balan, A. Scholl, *Nat. Nanotechnol.* **2014**, *9*, 514.
[16] C. Nisoli, V. Kapaklis, P. Schiffer, *Nat. Phys.* **2017**, *13*, 200.
[17] H. Stopfel, U. B. Arnalds, A. Stein, T. P. A. Hase, B. Hjörvarsson, V. Kapaklis, *Phys. Rev. Mater.* **2021**, *5*, 114410.
[18] N. Strandqvist, B. E. Skovdal, M. Pohlit, H. Stopfel, L. van Dijk, V. Kapaklis, B. Hjörvarsson, *Phys. Rev. Mater.* **2022**, *6*, 105201.
[19] A. Fernàndez-Pacheco, R. Streubel, O. Fruchart, R. Hertel, P. Fischer, R. P. Cowburn, *Nat. Commun.* **2017**, *8*, 15756.
[20] S. V. Grigoriev, K. S. Napolskii, N. A. Grigoryeva, A. V. Vasilieva, A. A. Mistonov, D. Y. Chernyshov, A. V. Petukhov, D. V. Belov, A. A. Eliseev, A. V. Lukashin, Y. D. Tretyakov, A. S. Sinitskii, H. Eckerlebe, *Phys. Rev. B* **2009**, *79*, 045123.
[21] A. A. Mistonov, I. S. Dubitskiy, I. S. Shishkin, N. A. Grigoryeva, A. Heinemann, N. A. Sapoletova, G. A. Valkovskiy, S. V. Grigoriev, *J. Magn. Magn. Mater.* **2019**, *477*, 99.
[22] K. Kobayashi, K. Ikuta, *Appl. Phys. Lett.* **2008**, *92*, 262505.
[23] V. Vieille, R. Pétrot, O. Stéphan, G. Delattre, F. Marchi, M. Verdier, O. Cugat, T. Devillers, *Adv. Mater. Technol.* **2020**, *5*, 2000535.
[24] J. M. De Teresa, A. Fernández-Pacheco, R. Córdoba, L. Serrano-Ramón, M. R. Ibarra, *J. Phys. D: Appl. Phys.* **2016**, *49*, 243003.
[25] M. Hunt, M. Taverne, J. Askey, A. May, A. Van Den Berg, Y.-L. D. Ho, J. Rarity, S. Ladak, *Materials* **2020**, *13*, 761.
[26] J. Fassbender, J. McCord, J. Magn. *Magn. Mater.* **2008**, *320*, 579.
[27] J. Fassbender, J. von Borany, A. Mücklich, K. Potzger, W. Möller, J. McCord, L. Schultz, R. Mattheis, *Phys. Rev. B* **2006**, *73*, 184410.
[28] L. Folks, R. E. Fontana, B. A. Gurney, J. R. Childress, S. Maat, J. A. Katine, J. E. E. Baglin, A. J. Kellock, *J. Phys. D: Appl. Phys.* **2003**, *36*, 2601.
[29] L. Ramasubramanian, A. Kákay, C. Fowley, O. Yildirim, P. Matthes, S. Sorokin, A. Titova, D. Hilliard, R. Böttger, R. Hübner, S. Gemming, S. E. Schulz, F. Kronast, D. Makarov, J. Fassbender, A. Deac, *ACS Appl. Mater. Interfaces* **2020**, *12*, 27812.
[30] Q. Li, M. Ying, in *Defect-Induced Magnetism in Oxide Semiconductors* (Eds: P. Kumar, J. P. Singh, V. Kumar), Woodhead Publishing, Cambridge, MA, USA **2023**.
[31] G. Muscas, R. Brucas, P. E. Jönsson, *Phys. Rev. B* **2018**, *97*, 174409.
[32] N. Gaur, S. Kundu, S. N. Piramanayagam, S. L. Maurer, H. K. Tan, S. K. Wong, S. E. Steen, H. Yang, C. S. Bhatia, *Sci. Rep.* **2013**, *3*, 1907.
[33] P. Ström, S. Ghorai, T. T. Tran, D. Primetzhofer, *J. Magn. Magn. Mater.* **2022**, *552*, 169207.
[34] E. T. Papaioannou, V. Kapaklis, A. Taroni, M. Marcellini, B. Hjörvarsson, *J. Phys. Condens. Matter* **2010**, *22*, 236004.
[35] T. P. A. Hase, M. S. Brewer, U. B. Arnalds, M. Ahlberg, V. Kapaklis, M. Björck, L. Bouchenoire, P. Thompson, D. Haskel, Y. Choi, J. Lang, C. Sánchez-Hanke, B. Hjörvarsson, *Phys. Rev. B* **2014**, *90*, 104403.
[36] H. Winter, A. Schüller, *Prog. Surf. Sci.* **2011**, *86*, 169.
[37] N. Dwivedi, A. K. Ott, K. Sasikumar, C. Dou, R. J. Yeo, B. Narayanan, U. Sassi, D. De Fazio, G. Soavi, T. Dutta, O. Balci, S. Shinde, J. Zhang, A. K. Katiyar, P. S. Keatley, A. K. Srivastava, S. K. R. S. Shankaranarayanan, A. C. Ferrari, C. S. Bhatia, *Nat. Commun.* **2021**, *12*, 2854.
[38] P. Ström, D. Primetzhofer, *J. Instrum.* **2022**, *17*, P04011.
[39] G. Nagy, H. J. Whitlow, D. Primetzhofer, *Nucl. Instr. Meth. Phys. Res. B* **2022**, *533*, 66.
[40] C. G. Ryan, D. R. Cousens S. H. Sie, W. L. Griffin, *Nucl. Instr. Meth. Phys. Res. B* **1990**, *49*, 271.
[41] D. Nečas, P. Klapetek, *Cent. Eur. J. Phys.* **2012**, *10*, 181.

© 2024 Wiley-VCH GmbH

18626270, 2024, 8, Downloaded from https://onlinelibrary.wiley.com/doi/10.1002/pssr.202400053 by Uppsala University Library, Wiley Online Library on [12/08/2024]. See the Terms and Conditions (https://onlinelibrary.wiley.com/terms-and-conditions) on Wiley Online Library for rules of use; OA articles are governed by the applicable Creative Commons License